JGR Space Physics

RESEARCH ARTICLE
10.1029/2024JA033083

Effects of a Solar Flare on Global Propagation of Extremely Low Frequency Waves

M. Ostrowski[1], M. Gołkowski[2], J. Kubisz[1], Z. Nieckarz[3], A. Michalec[1], J. Mlynarczyk[4], J. Lichtenberger[5,6], and A. Maxworth[7]

[1]Astronomical Observatory, Jagiellonian University, Kraków, Poland, [2]Department of Electrical Engineering, University of Colorado Denver, Denver, CO, USA, [3]Marian Smoluchowski Institute of Physics, Jagiellonian University, Kraków, Poland, [4]Institute of Electronics, AGH University of Kraków, Kraków, Poland, [5]Department of Geophysics and Space Sciences, Eötvös University, Budapest, Hungary, [6]HUN-REN-ELTE Space Research Group, Budapest, Hungary, [7]Department of Engineering, University of Southern Maine, Gorham, ME, USA

Key Points:

- Applying new data analysis, we show solar flare effects on the extremely low frequency emissions from global lightning
- An M-class solar flare causes decreased attenuation and increased group velocity in ELF band
- The measured propagation parameters agree with theoretical modeling and suggest global remote sensing capabilities using ELF observations

Correspondence to:
M. Ostrowski,
michal.ostrowski@uj.edu.pl

Citation:
Ostrowski, M., Gołkowski, M., Kubisz, J., Nieckarz, Z., Michalec, A., Mlynarczyk, J., et al. (2024). Effects of a solar flare on global propagation of extremely low frequency waves. *Journal of Geophysical Research: Space Physics*, *129*, e2024JA033083. https://doi.org/10.1029/2024JA033083

Received 19 JUL 2024
Accepted 21 NOV 2024

Author Contributions:
Conceptualization: M. Ostrowski, M. Gołkowski, J. Kubisz, Z. Nieckarz
Data curation: J. Kubisz, A. Michalec, J. Lichtenberger, A. Maxworth
Formal analysis: M. Ostrowski, M. Gołkowski, J. Kubisz, Z. Nieckarz
Investigation: M. Ostrowski, M. Gołkowski, Z. Nieckarz, A. Michalec
Methodology: M. Ostrowski, M. Gołkowski, J. Kubisz, Z. Nieckarz
Resources: J. Kubisz, J. Lichtenberger, A. Maxworth
Software: M. Gołkowski, J. Kubisz, Z. Nieckarz
Supervision: M. Ostrowski
Validation: M. Ostrowski, M. Gołkowski, J. Kubisz, Z. Nieckarz
Visualization: M. Ostrowski, M. Gołkowski, J. Kubisz, Z. Nieckarz
Writing – original draft: M. Ostrowski, M. Gołkowski
Writing – review & editing: M. Ostrowski, J. Kubisz, Z. Nieckarz, A. Michalec, J. Lichtenberger

Abstract Solar flares have profound impacts on the lower ionosphere and long-distance radio propagation. Extremely low frequency (ELF: 3–3,000 Hz) waves are challenging to observe and experience unique interactions with the lower ionosphere. The primary natural sources of ELF waves are thunderstorm lightnings across the globe. Using a newly developed azimuth determination technique and improved observation hardware we show that ELF attenuation in the Earth-Ionosphere spherical cavity decreases and propagation velocity increases under the influence of an M-class solar flare. Using a two-parameter model of the lower ionosphere, the observations are shown to be consistent with increased electron density and sharper gradients in the D-region resulting from X-ray radiation. The sharper electron density gradient is primarily responsible for the propagation velocity increase, suggesting a unique capability that ELF observations can bring to global remote sensing of the lower ionosphere under space weather perturbations.

Plain Language Summary Solar flares are large emissions of energy from the Sun that hit the Earth with X-rays and ultraviolet emissions. A solar flare has significant effects on the upper atmosphere of the Earth, known as the ionosphere. The solar flare X-ray radiation leads to an increase in free electron density in the lower ionosphere by ionizing more of the neutral atmosphere. This increase in electron density can in turn have profound effects on long range radio wave propagation. In this study we focus on observations of Extremely Low Frequency (ELF: 3–3,000 Hz) waves and how they are affected by a solar flare. ELF waves are challenging to observe and generate. The primary source of ELF radiation on Earth is thunderstorm lighting. We use a new analysis technique and improved observation hardware to show that ELF waves propagate more effectively and faster under the influence of a solar flare. The unique response of ELF waves to solar flares can be leveraged in global monitoring of the lower ionosphere which is important for a wide range of communication technologies.

1. Introduction

Solar flares are sources of large eruptions of electromagnetic radiation from the Sun lasting from minutes to hours. The increased level of X-ray and extreme ultraviolet radiation results in increased ionization in the lower layers of the ionosphere on the sunlit side of Earth (Mitra, 1975; Tsurutani et al., 2009). Solar flare events are known to significantly affect propagation of all radio waves that experience reflection from the ionosphere. This covers the ELF (3–3,000 Hz) band up to the HF (3–30 MHz) band. The primary effect of a solar flare on the ionosphere is to significantly increase the electron density in the lowest layer, the D-region. For waves in the HF band, which reflect from the F-region of the ionosphere, the increased D–region density leads to greater attenuation. In extreme cases, a solar flare can cause significant deterioration of HF propagation conditions in what is known as radio blackout. For the VLF band, the reflection occurs in the D-region and solar flare conditions cause a decrease in reflection height by several kilometers. Moving the reflection height to a lower altitude where electron neutral scattering conditions are more prominent leads to observed phase advance and increased attenuation in the lower VLF band (<16 kHz) and decreased attenuation in the upper VLF band (>16 kHz) (Anderson et al., 2020; McRae & Thomson, 2004; Schmitter, 2013; Thomson & Clilverd, 2001; Wenzel et al., 2016).

The effects of solar flares on ELF waves differ from the effects on the VLF band (Gołkowski et al., 2018). The long wavelength of ELF waves leads to a partial decoupling of electric and magnetic fields in the lower ionosphere. The varying penetration depth of the two fields means that these waves experience significant group

velocity dispersion and complicated attenuation dependence despite propagating in the lowest order TEM mode in the Earth-ionosphere waveguide.

Using recently developed methods of azimuth determination (Kubisz et al., 2024) and improved ELF recording hardware, we show with greater precision than in past work that ELF waves experience a significant decrease in attenuation and accompanied increase in group velocity with the occurrence of a solar flare. This confirms the unique utility of ELF waves in ionospheric remote sensing on a global scale.

2. ELF Observations and the Azimuth Derivation Procedure

Extremely low frequency (ELF) electromagnetic waves are regularly generated by lightning discharges in the atmosphere. Due to long propagation paths in the spherical earth-ionosphere cavity, ELF waves generated across the globe can be studied even with a single site detector (see e.g. a book by Nickolaenko & Hayakawa, 2002 or a recent review by Liu et al., 2023). In the present study we used a magnetic sensor ELA11 installed in a geophysical station Hylaty (Kulak et al., 2014) in the South-East of Poland (49.2°N, 22.5°E) which uses 18-bit digital electronics and orthogonal east-west (EW) and north-south (NS) magnetic antennas to continuously monitor natural electromagnetic phenomena from 0.03 to 1,000 Hz. The sampling frequency is 3 kHz, but the anti-aliasing roll-off begins at 700 Hz. To minimize interference from the 50 Hz electric power lines we apply a third-order bandstop Butterworth filter, as described in detail in Kubisz et al. (2024). The ELA11 sensor has improved timing accuracy over the previous ELA10 hardware (Kulak et al., 2014) resulting from the higher sampling frequency and more frequent GPS correction of sampling clock.

Our analysis approach, described by Kubisz et al. (2024), allows parametrized investigation of azimuths of individual electromagnetic impulses within the diverse ELF spectrum. Thus, the method allows to identify the azimuths of multiple varying thunderstorm centers on the globe, with the exception of periods when the ELF spectrum is fully dominated by strong local thunderstorms.

Following Kubisz et al. (2024), at each following time instant, t_i, we derive the signal azimuth of arrival, A_i, measured from the north toward the east direction. We use the recorded signal changes in our NS and EW antennas between time instants t_i and t_{i+n} in the expression $\tan(A_{(i,n)}) = \Delta B_{\mathrm{NS}(i,n)}/\Delta B_{\mathrm{WE}(i,n)} = -\Delta B_{\mathrm{NS}(i,n)}/\Delta B_{\mathrm{EW}(i,n)}$, where $\Delta B_{(i,n)} = B_{(i+n)} - B_{(i)}$ is the difference between two signal measurements from a given magnetic antenna, NS or EW. Depending on positive or negative values of the derived $\Delta B_{(i,n)}$ we obtain azimuths in the range $(-180°, +180°)$. One should note here, as discussed in detail in Kubisz et al. (2024), that if–using our procedure–the increasing amplitude part of a single impulse yields the azimuth A, then the azimuth derived from the declining part of this impulse will be $A \pm 180°$. Due to this feature any considered thunderstorm center at the azimuth A is generally represented here by measurements both in A and $A \pm 180°$, though there may be some differences in features due to temporal asymmetry of impulses. One should also note that without an electric field measurement or information on the lightning source it is impossible to overcome the 180° ambiguity in derived azimuth of an impulse using a single sensor with two perpendicular magnetic antennas only. When selecting signals for the azimuth derivation, we limit their magnitudes to pre-defined values for any given n by selecting the minimum and maximum limits $r_{\min}$ and $r_{\max}$ for the signal change parameter $r = \sqrt{\Delta B_{NS}^2 + \Delta B_{EW}^2}$. The measured signal (before performing the 50 Hz filtering) is provided by natural numbers in the digital ELA11 sensor units, with a 1 pT magnetic field change equivalent (in September 2023) to 9.68 sensor units ("[s.u.]"; 1 s.u. = 0.1033 pT). Thus, using the parameters n and r, one is able to filter derived azimuths in terms of the temporal and amplitude characteristics of the wave source as well as–to some degree–its distance from the receiving station.

The described differential method provides an instantaneous azimuth of the wave reaching the sensor at a given moment. Using $n = 1$, the azimuths correspond to time bins of approximately 0.33 ms. The measured impulse from a single discharge can last several milliseconds and thus with a global lightning frequency of 50–100 per s, the superposition of different impulses in the data is limited and one can expect to obtain reliable measurements of azimuths from different thunderstorms. The method proves to be quite powerful, allowing for separation and time tracking of signal azimuths from multiple thunderstorms simultaneously, due to high dynamics of the applied magnetic sensor as well as a wide range of ELF impulse amplitudes analyzed using a single procedure.

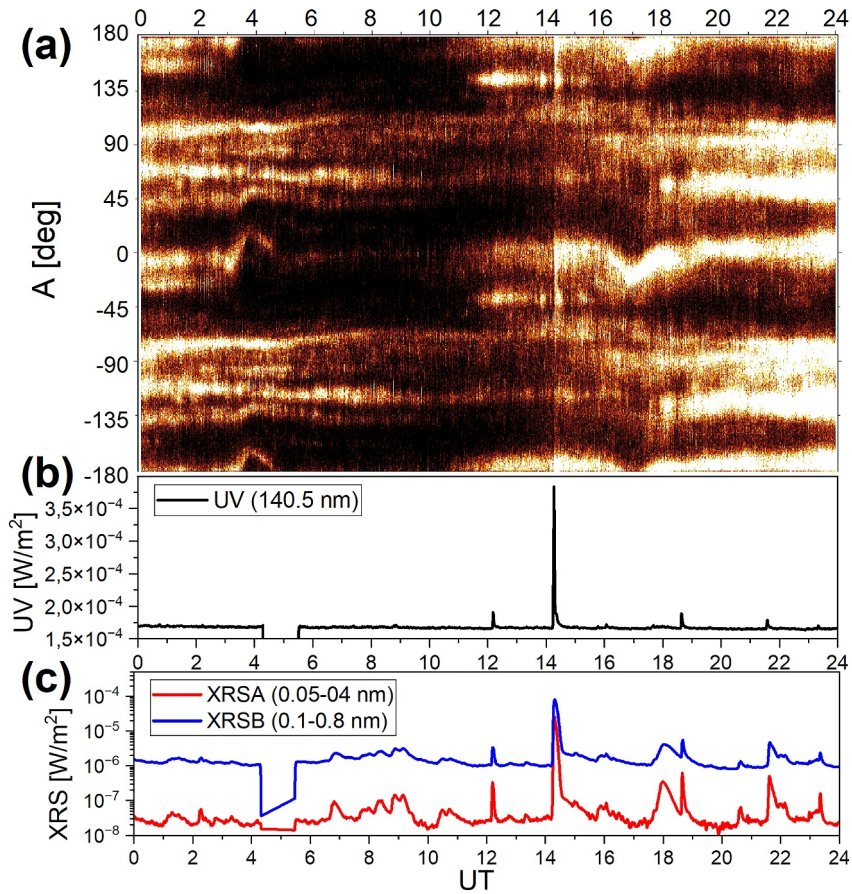

Figure 1. Top (Panel a): The azimuth distribution in the Hylaty station as measured on 20 September 2023, derived for $n = 1$, $r_{min} = 40$ [s.u.], $r_{max} = 200$ [s.u.]. Bottom: Solar ionizing radiation fluxes on the same day observed from the Extreme Ultraviolet (EV; Panel (b) and X-ray Sensors (XRS; Panel (c) on a GOES-16 satellite with 1 min time resolution (https://www.ngdc.noaa.gov/stp/satellite/goes-r.html). The instant brightening in panel (a) at the time of the solar flare is caused by an increase in observed lightning impulses arriving at the receiver.

3. Signature of a Solar Flare Emission in the ELF Data

In the present study we analyze data during September 2023, when local thunderstorm activity near the Hylaty station was limited. This allows monitoring of the variations of ELF signal azimuths from numerous distant thunderstorm centers without local perturbations. As demonstrated by Kubisz et al. (2024), depending on the parameters (n, r_{min}, r_{max}) selected in the algorithm for determination of ELF wave azimuths, one can selectively include or exclude signals from different thunderstorms, either sharp peaks from "nearby" lightning, or dispersed and diminished signals varying with the source amplitude and distance.

Figure 1 shows a characteristic daily distribution of measured azimuths on the selected day of Sept. 20th, 2023. The wavy structure of azimuth fluctuations close to local sunrise (~4:00 UT) and sunset (~17:00 UT) is due to passage of the day-night terminator. The key feature we bring attention to here is an unexpected "brightening" on the plot observed simultaneously at several different azimuths just after 14:15 UT. The brightening, indicating an increase of azimuth measurement frequency for the selected $n = 1$, $r_{min} = 40$ [s.u.] and $r_{max} = 200$ [s.u.], is most prominent for azimuths around ~0° and ~180° which correspond (see explanations above) to a direction due south, near the lightning hotspot of sub-Saharan Africa which is expected to be active at this time. The event occurred following the solar ionizing radiation burst released by the M8.2 solar flare (14:11–14:25 UT) with X-ray flux maximum at 14:18 UT, as plotted on Figures 1 and 2.

When inspecting Figure 1, one should note that the presented color scale of a panel (a) is selected in a way to best visualize different thunderstorm azimuth structures, and it is not related in a simple way to the measured

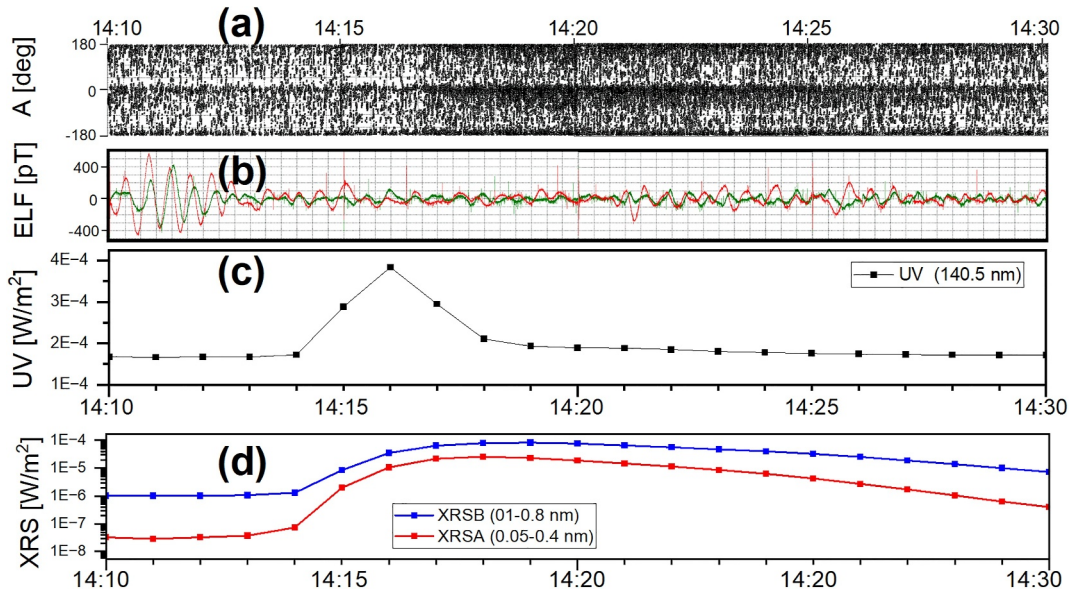

Figure 2. ELF electromagnetic measurements (Panels (a) and (b) on the top) versus the solar flare ionizing emissions (Panels (c) and (d) in the bottom) in the time range 14:10–14:30 UT. In the Panel (b), we show the ELF measurements in [pT] from EW (green) and NS (red) antennas, while in Panel (a) the measured azimuths A [°] derived for the parameters (n = 1, r_{min} = 30 [s.u.], r_{max} = 5,000 [s.u.]) are presented. In the bottom two panels of the figure the respective solar ionizing radiation fluxes in the units of [W/m^2] are presented in the same time range for UV (Panel c) and XRS (Panel d) sensors on a GOES-16 satellite with 1 min time resolution (https://www.ngdc.noaa.gov/stp/satellite/goes-r.html).

thunderstorm electromagnetic signal intensity. The brightening is correlated to an increased number of azimuth derivations of arriving lightning impulses, but subject to the parameters of the azimuth determination algorithm. The number of azimuth measurements presented on the plot can significantly vary depending on the parameters (n, r_{min}, r_{max}) selected for the analysis, but also on the intensity of impulses with measurements satisfying $r_{min} < r < r_{max}$. Thus, to make the presented structures clear for the reader we use a procedure wherein we multiply the derived azimuth numbers in all time-azimuth bins (75 s, 1°) on the plot by an arbitrary selected number, and subtract another arbitrary number to shift the zero level of the distribution. Such interactive corrections of the picture are applied in a way intended to make the tracked thunderstorms at different azimuths bright enough to be well visible, but also to be well resolved from the other thunderstorm structures. It is also worth noting that in the applied algorithm each impulse that is symmetric in time will yield a "symmetric" azimuth measurement of A and $A \pm 180°$, from the growing part of the impulse and the declining part, respectively. Asymmetries observed at the plot show that it is not always the case due to the electric current variability in the source discharge, interference of other waves, as well as signal dispersion along long propagating paths. Together, these processes lead to asymmetric temporal structures of the analyzed ELF impulses.

In Figure 2 we compare in detail our ELF data with the profile of the flare's ionizing fluxes measured by GOES-16. When inspecting the figure, one should note that high amplitude perturbations below 1 Hz visible in Panel (2b) are not related to the studied thunderstorm activities reflected in measured impulses with time scales of several milliseconds depicted in Panel (2a), these measured impulses cannot be recognized by eye in Panel (2b). Even rough inspection of the data plot reveals a significant increase of electromagnetic impulses' occurrence following the maximum emission of the UV flare but growing and decaying approximately in phase with the X-ray emission of the flash. There is a significant increase in the number of measured azimuths which is manifested as an increased number of black dots in the Panel 2a, indicating increase of impulse occurrence within the (wide), r_{min} = 30 [s.u.], r_{max} = 5,000 [s.u.], parameter range selected for azimuth derivation. On the figure one may note a time delay on the order of a few minutes, between the increase in activity measured in ELF and the UV ionizing radiation spike, but the process is well fitted in time at and after the X-ray emission maximum, but initiates with ∼2 min delay with respect to the X-ray radiation flux. As discussed below, the increase in lightning observations is interpreted to result from decreased attenuation in the Earth-ionosphere wave guide caused by additional

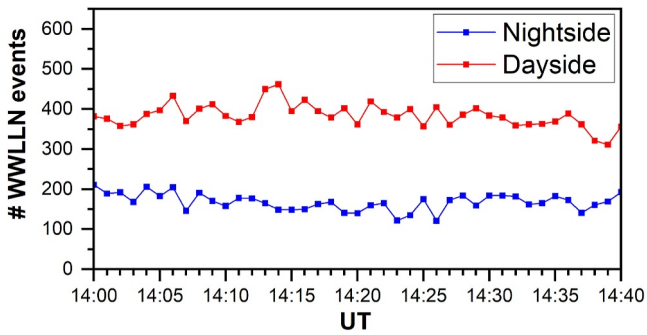

Figure 3. Recorded WWLLN events in one-minute intervals near the studied solar flare on 20 September 2023, 14:18 UT. Number of recorded strokes are presented separately for the dayside (red) and the nightside (blue).

ionization of the low layers of the ionosphere by the solar flare X-rays. The decreased attenuation causes a larger number of signatures of low and medium amplitude discharges to be detected by the algorithm.

To verify the above finding with an independent data sample, we analyzed the lightning frequency recorded in VLF measurements by the WWLLN lightning detection network (https://wwlln.net) (Kaplan & Lau, 2022). In Figure 3, one can see the number of lightning events per minute detected by WWLLN in the 40 min time span including the studied flare period. We plot separately the number of lightning events on the day and night sides of the Earth since only the day side is ionized by the solar flare. There is no indication of any increase of lightning occurrence, neither on the day- nor on the nightside. Although Anderson et al. (2020) discuss decreasing detection efficiency of the WWLLN network under solar flare conditions due to increased VLF attenuation, the large number of stations and the fact that WWLLN focuses on large amplitude discharges can be assumed to minimize any effect on this day with the moderate M8.2 flare.

Let us inspect the ELF measurements in more detail in short (below ∼1 s) time scales, allowing identification of individual impulses contributing to the measurements. In Figure 4, we plot two sections of our ELF measurements with additional demarcation of all WWLLN identified impulses occurring in the considered time ranges. One may note that the number of all lightning generated impulses which can be identified in the plot is much larger than the number of impulses identified by WWLLN. This fact confirms the previous findings that WWLLN is primarily

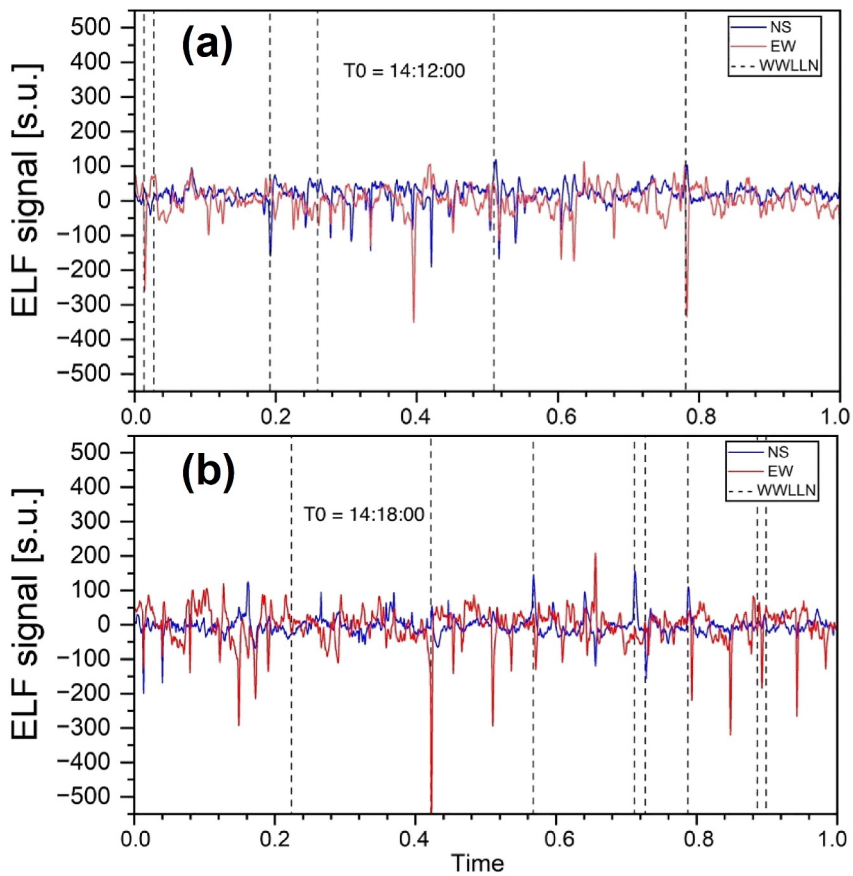

Figure 4. Magnetic sensor ELA11 measurements from EW and NS antennas, with filtered out 50 Hz power line signatures, for a one second time period starting at 14:12:00 UT (before a flare; Panel a) and another 1 s period at 14:18:00 UT (during the flare X-ray flash maximum; Panel b). Vertical dashed lines indicate the derived times (assuming an impulse propagation velocity of 0.85°C) for expected detection of the WWLLN events occurring in the considered time range.

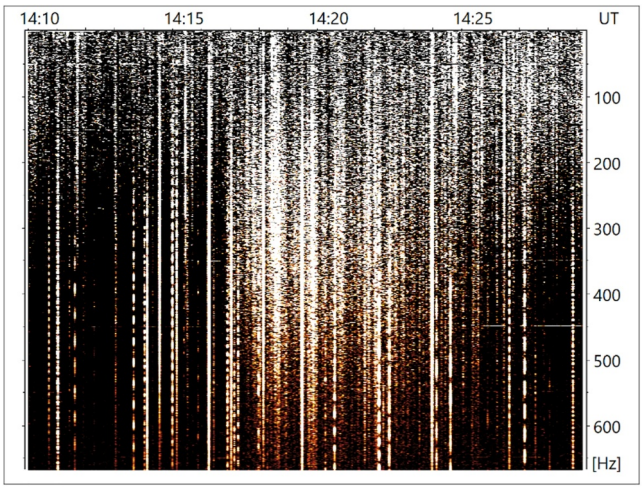

Figure 5. Time variation of the difference between the 10.8 s power spectrum and the mean spectrum in a full presented time range. The measured deviations are presented for each spectrum at each consecutive second, together 1,150 vertical data lines using the considered overlapped spectra. An extended "plateau" is visible of increased ELF spectral power ranging from the Schumann Resonances' frequencies up to or even above 600 Hz, with gradual shift of above-the-average wave power to somewhat lower frequencies, below 300 Hz at the plot time limit.

sensitive to large lightning events (Hutchins, Holzworth, Brundell, & Rodger, 2012). Thus, the majority of impulses revealed in our measurements are possibly generated by smaller and/or closer lightnings than the WWLLN ones. However, a slightly larger density of impulses can be observed in the ELF data for the period during the flare, which we interpret here as resulting from lower wave attenuation allowing for registering individual impulses from larger distances and/or lower amplitude lightning discharges.

Of course, the observed increased occurrence of discharges due to lowered ionospheric attenuation should also be accompanied with higher instantaneous energy content in the global resonator. This increase can be observed as an increase in the dynamic power spectrum of the measured ELF signal. Figure 5 shows a variation of the ELF power spectrum for the studied time range 14:10–14:29 UT. In our procedure–arbitrary selected to diminish fluctuations at the plot–the spectra were calculated every 1 s using a following 10.8 s time window. Thus, with each spectrum shifted in time by 1 s from the previous spectrum, we keep 9.8 s of common data for successive spectra smoothing the spectral fluctuations in shorter time scales. Then, a mean 10.8 s power spectrum was derived from all spectra within the studied time range, and it was subtracted from all successive power spectra. These differences are presented in Figure 5. In the figure one can note a time range (after 14:17 UT) with increased power extending from the low frequency Schumann Resonances range up to above 600 Hz. As expected from the flare X-ray light curve with more numerous impulses and related azimuth determinations during the flare, the additional (above average) power in the spectrum is seen in Figure 5 as a diffuse plateau structure from approximately 14:17 UT, increasing intensity and spectral range to the X-ray flash maximum at minutes 18–20, and then slowly diminishing and shifting to lower frequencies up to the plot edge at 14:29 UT. It is worth noting that neither the time domain analysis (Figures 2 and 4), nor the spectrum analysis (Figure 5), are as effective as the azimuth derivations (Figure 1) in clearly and unambiguously showing the effects of the solar flare by simultaneous modification of signals from numerous different thunderstorms on Earth on the azimuth plot.

As first presented by Gołkowski et al. (2018) a solar flare is expected to lead to an increase in ELF group velocity since the density gradient of the lower ionosphere is increased. Using WWLLN lightning events registered by our magnetic sensor in the station Hylaty one can verify these theoretical results for the ionospheric effects resulting from the studied X-ray flash. Following Nieckarz et al. (2011) we identified WWLLN events in the ELF data, for events at distances from 5,000 up to 9,000 km and within the geographic azimuth range of ±20° near $A = 180°$. Knowing the WWLLN event time and position on Earth we derived the ELF impulse propagation velocity. Note, that here we compute the considered azimuth values in a different way in comparison to the procedure above for Figure 1, by fitting the considered impulse maxima at NS and EW antenna signals and using these values in azimuth derivation. In Figure 6 the derived group velocity is compared to accompanying solar flare ionizing fluxes in UV and X-rays. One may note a sharp increase in propagation velocity during the flare, from a normal daily value close to 0.86°C up to 0.90°C–0.91°C coinciding with the X-ray flux maximum, and then slower decrease to the unperturbed value, with some evidence of sustained decrease to 0.84°C after 14:30 UT. There is a delay between the rising part of the X-ray flux and the rise of ELF group velocity of 1–3 min as is expected for ionospheric density changes in response to solar flares (Mitra, 1974, pp. 106–113). The data presented at Figure 6, with some misidentified impulses occurring as outliers or even outside the presented range, are preliminary results of an intended wide analysis of the WWLLN impulses in ELA11 data.

4. Analysis With Model of D-Region Response

We compare our observational results on attenuation and propagation velocity with an analytical model of the expected D-region response to a solar flare. A large body of prior work in the VLF band has utilized a 2-parameter (h'–a reference height, β–the electron distribution steepness parameter) D-region ionosphere introduced by Wait and Spies (1964) (Cummer et al., 1998; Gołkowski et al., 2021; Han & Cummer, 2010; Lay et al., 2014;

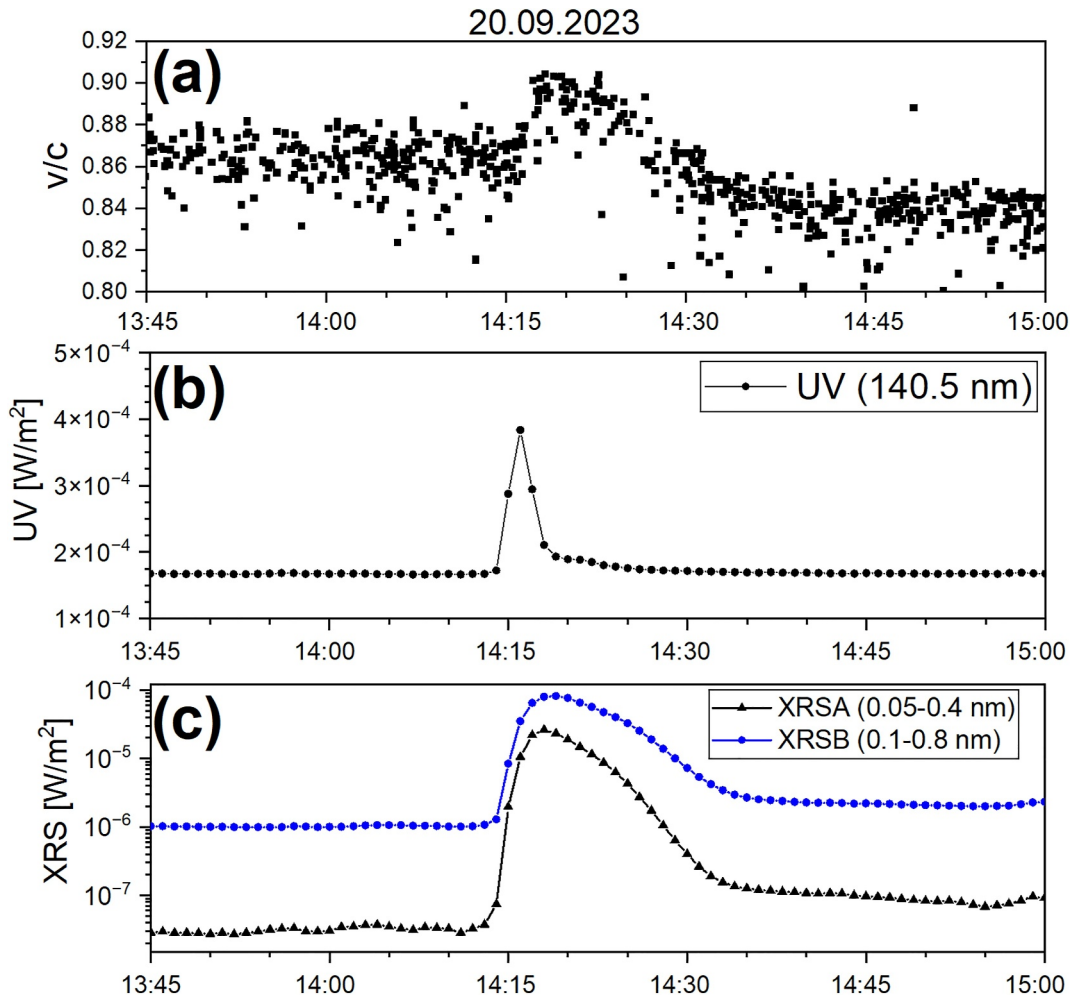

Figure 6. Distribution of propagation velocities *v/c* for WWLLN impulses identified in our ELF data. For the date of 20 September 2023, the data fitted from 13:30 UT till 15:00 UT are presented in a Panel (a), with a ∼10 min' v/*c* increase around 14:20, similar in shape to the X-ray flash profile presented in the Panel (c). A 140.5 nm UV flux is also provided in the Panel (b) for comparison. The UV and X-ray data are taken from the GOES-16 repository (https://www.ngdc.noaa.gov/stp/satellite/goes-r.html).

Schmitter, 2013; Thomson et al., 2005). In this model the electron density, N, and electron-neutral collision frequency, ν, are given as function of altitude z

$$N(z) = N_0 e^{-\beta h'} e^{(\beta-0.15)z}; \quad N_0 = 1.43 \times 10^{13}\ [\mathrm{m}^{-3}]$$
$$\nu(z) = \nu_0 e^{-0.15z}; \quad \nu_0 = 1.86 \times 10^{11}\ [\mathrm{s}^{-1}]$$

To capture the effect of the solar flare on the D-region we use a model put forth by Han and Cummer (2010) and Schmitter (2013) and successfully employed in the ELF band by Gołkowski et al. (2018). The values of h', β change from their initial unperturbed values h_0', β_0 as

$$h' = h'_0 + dh' = h'_0 - 5.5 \log_{10}\left(\frac{X_{flux}}{10^{-6}}\right)$$
$$\beta = \beta_0 + (\beta_m - \beta_0)\left[1 - \exp\left(2dh'/5.5\right)\right],$$

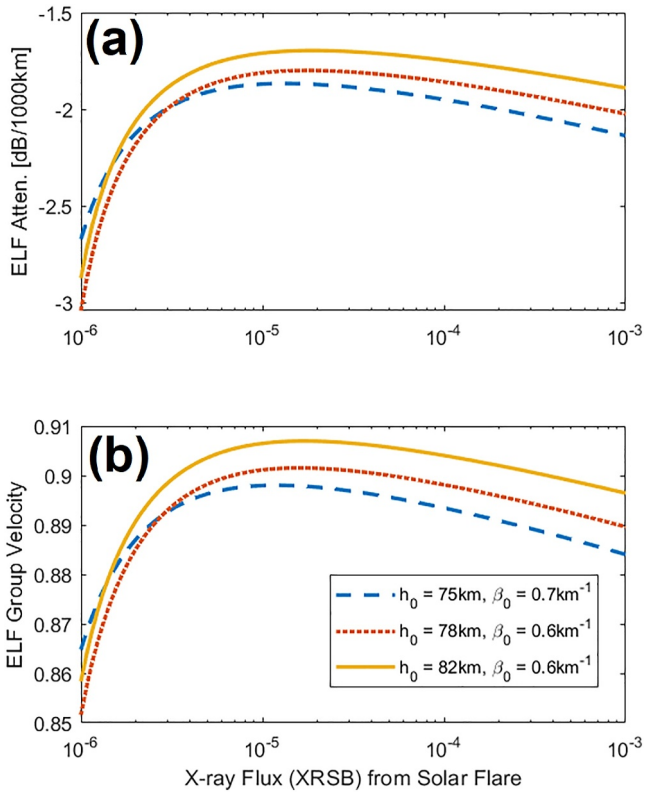

Figure 7. Expected attenuation (Panel a) and group velocity (fraction of the speed of light, Panel b) for 450 Hz for three different daytime D-region conditions. The attenuation decreases and group velocity increases in agreement with observations of increased lightning events and shorter propagation time.

The above model works for solar flares where the soft X ray flux, $X_{flux} > 10^{-6}$ W/m^2, in other words *C*, *M*, and *X* class flares. The parameter β_m is the maximum saturation value which we take to be 1.1 km^{-1}. ELF propagation can be expressed with complex phasor expressions for the *E* and *B* fields as a function of distance, ρ, in the form

$$E, B \sim \frac{1}{\sqrt{\rho}} e^{jkS_0\rho}$$

where

$$S_0^2 = \frac{\ln\left(\frac{\omega\varepsilon_0 m_e \nu_0}{N_0 q_e^2}\right) + \beta h' + j\pi}{\ln\left(\frac{m_e \nu_0 \beta^2}{4\omega\mu_0 N_0 q_e^2}\right) + \beta h' - j\pi}$$

and m_e, ε_0, μ_0 are electron mass, permittivity and permeability of free space, respectively. The above is based on Greifinger and Grifinger (1978) solutions applied to the two parameter D-region ionosphere (Gołkowski et al., 2018). Figure 7 shows results of attenuation and group velocity for a 450 Hz wave as function of incident X ray flux for three different initial conditions of the D-region. The initial *h*' values are typical daytime parameters (McRae & Thomson, 2000), the initial β values were chosen to match the ambient propagation velocity of ~0.86°C and while they are higher than daytime values derived by McRae and Thomson (2000), they are still lower than daytime values of 0.9 km^{-1} reported by Lay et al. (2014). The 450 Hz frequency is in the middle of the active band of the ELA11 receiver. We see a significant decrease in attenuation and increase in group velocity with X ray flux from 10^{-6} to 10^{-5} [W/m^2] and flattening for further X-ray flux. The values of the ELF group velocity and attenuation are in general agreement with the observations. While the attenuation values cannot be compared directly due to uncertainty of the source amplitudes, the propagation velocity change from ~0.86°C to ~0.90°C can be matched rather well. Since ELF group velocity can be approximated as proportional to steepness parameter, β, the sustained lower value of propagation velocity after the solar flare (0.84°C) suggests that the ionospheric gradients did not recover to their previously higher value (associated with propagation velocity of 0.86°C).

5. Summary and Discussion

Our analysis of ELF electromagnetic wave measurements in the Earth–Ionosphere resonance cavity revealed an effect of the solar flare increasing the observed ELF thunderstorm lightning activity at wide range of azimuths, in particular from the southern direction, likely associated with lightnings in Africa. We note that the increased activity is observed in ELF including small and intermediate lightning discharges, while there are no visible effects for high amplitude discharges recorded by WWLLN (Hutchins, Holzworth, Rodger, & Brundell, 2012). The increased ELF activity is evident in the time and frequency domains but is most apparent using the azimuth determination technique of Kubisz et al. (2024), which allows for sorting the ELF spectrum by direction, temporal structure and also amplitude of observed signals. Also observed is a very clear increase in ELF group velocity coinciding with the ionizing X-ray flux. This increase in group velocity has been observed before (Gołkowski et al., 2018), but here the resolution of the observation is improved due to the improved timing of the ELA11 recording station.

The observations of both the decreased attenuation and increased group velocity match well the expected ionospheric changes predicted for the two parameter (*h*', β) model of the D-region ionosphere and its expected changes under the influence of solar X-ray flux. Attenuation values are difficult to compare quantitatively since

the source amplitude characteristics are not known accurately, but group velocity changes are well matched in absolute values and total change for the selected initial conditions.

The effect of the solar flare is to lower the effective height (h') and increase the sharpness or gradient (β) of the electron density. The solar flare effect is thus different from the diurnal-day-night changes of the D-region where both h', β typically increase at night and decrease during the day. Since the ELF group velocity is more sensitive to the density gradient (Gołkowski et al., 2018), we see an initial increase of ELF group velocity to values that would be normally associated with nighttime, even though the overall density has exceeded even the daytime values. The theoretical model presented here is appropriate only for large X-ray fluxes above 10^{-6} W/m^2 and does not include the effects of D-region recovery. The recovery process of the D-region from ionizing perturbation can be complicated since a large number of chemical processes occur simultaneously with electron recombination and attachment (Kotovsky & Moore, 2016; Verronen et al., 2005). As the electron density decreases during the recovery phase, the relative rates of h' and β changes are expected to have a unique ELF group velocity signature. One can see evidence in Figure 6 that the group velocity returns to a lower level, below that before the event, after the main X-rays have subsided. This suggests the D-region does not simply return to its pre-event state and in particular the electron gradients may exhibit complex structure and dynamics.

The present study highlights the utility of high-fidelity ELF observations in conjunction with lightning detection networks. The unique properties of ELF waves can be exploited in global monitoring of the D-region ionosphere which is a longstanding challenge and goal (Anderson et al., 2020; Gołkowski et al., 2021).

Data Availability Statement

The ELF measurements used in this publication are available on-line in Kubisz and Mlynarczyk (2024).

Acknowledgments
Authors are grateful to Astronomical Observatory of the Jagiellonian University for continues support of ELF research and operation of the WERA magnetic sensors' array. The development of ELA11 sensor has been supported by the National Science Centre, Poland, under Grant 2015/19/B/ST10/01055. This research was funded in part by the National Science Centre, Poland, under Grant 2023/49/B/ST9/02777 (MO and JK) and within the project 2023/49/B/ST9/00142 (ZN). Mark Golkowski was supported by National Science Foundation Awards AGS 2312282 and AGS 2320259 to University of Colorado Denver. János Lichtenberger was supported by TKP2021-NVA-29 project, that has been implemented with the support provided by the Ministry of Culture and Innovation of Hungary from the National Research, Development and Innovation Fund, financed under the TKP2021-NVA funding scheme.

References

Anderson, T. S., McCarthy, M. P., & Holzworth, R. H. (2020). Detection of VLF attenuation in the Earth-ionosphere waveguide caused by X-class solar flares using a global lightning location network. *Space Weather*, *18*(3), e2019SW002408. https://doi.org/10.1029/2019SW002408

Cummer, S. A., Inan, U. S., & Bell, T. F. (1998). Ionospheric D region remote sensing using VLF radio atmospherics. *Radio Science*, *33*(6), 1781–1792. https://doi.org/10.1029/98RS02381

Gołkowski, M., Renick, C., & Cohen, M. B. (2021). Quantification of ionospheric perturbations from lightning using overlapping paths of VLF signal propagation. *Journal of Geophysical Research: Space Physics*, *126*(5), e2020JA028540. https://doi.org/10.1029/2020JA028540

Gołkowski, M., Sarker, S. R., Renick, C., Moore, R. C., Cohen, M. B., Kułak, A., et al. (2018). Ionospheric D region remote sensing using ELF sferic group velocity. *Geophysical Research Letters*, *45*(23), 12–739. https://doi.org/10.1029/2018GL080108

Greifinger, C., & Grifinger, P. (1978). Approximate method for determining ELF eigenvalues in the earth-ionosphere waveguide. *Radio Science*, *13*(5), 831–837. https://doi.org/10.1029/RS013i005p0083

Han, F., & Cummer, S. A. (2010). Midlatitude daytime D region ionosphere variability on hourly to monthly time scales. *Journal of Geophysical Research*, *115*(A9). https://doi.org/10.1029/2010JA015715

Hutchins, M. L., Holzworth, R. H., Brundell, J. B., & Rodger, C. J. (2012). Relative detection efficiency of the world wide lightning location network. *Radio Science*, *47*(6), RS6005. https://doi.org/10.1029/2012RS005049

Hutchins, M. L., Holzworth, R. H., Rodger, C. J., & Brundell, J. B. (2012). Far-field power of lightning strokes as measured by the world wide lightning location network. *Journal of Atmospheric and Oceanic Technology*, *29*(8), 1102–1110. https://doi.org/10.1175/JTECH-D-11-00174.1

Kaplan, J. O., & Lau, K. H.-K. (2022). World wide lightning location network (WWLLN) global lightning climatology (WGLC) and time series, 2022 update. *Earth System Science Data*, *14*(12), 5665–5670. https://doi.org/10.5194/essd-14-5665-2022

Kotovsky, D. A., & Moore, R. C. (2016). Photochemical response of the night-time mesosphere to electric field heating—Recovery of electron density enhancements. *Geophysical Research Letters*, *43*(3), 952–960. https://doi.org/10.1002/2015GL067014

Kubisz, J., Gołkowski, M., Mlynarczyk, J., Ostrowski, M., & Michalec, A. (2024). New method for determining azimuths of ELF signals associated with the global thunderstorm activity and the Hunga Tonga volcano eruption. *Journal of Geophysical Research: Atmospheres*, *129*(4), e2023JD040318. https://doi.org/10.1029/2023JD040318

Kubisz, J., & Mlynarczyk, J. (2024). A set of measurement data from the ELA11 magnetometer from September, 2023. *Hylaty Station, Poland [Dataset]*. https://doi.org/10.57903/UJ/LOGPP8

Kulak, A., Kubisz, J., Klucjasz, S., Michalec, A., Mlynarczyk, J., Nieckarz, Z., et al. (2014). Extremely low frequency electromagnetic field measurements at the Hylaty station and methodology of signal analysis. *Radio Science*, *49*(6), 361–370. https://doi.org/10.1002/2014RS005400

Lay, E. H., Shao, X.-M., & Jacobson, A. R. (2014). D region electron profiles observed with substantial spatial and temporal change near thunderstorms. *Journal of Geophysical Research: Space Physics*, *119*(6), 4916–4928. https://doi.org/10.1002/2013JA019430

Liu, J., Huang, J., Li, Z., Zhao, Z., Zeren, Z., Shen, X., & Wang, Q. (2023). Recent advances and challenges in Schumann resonance observations and research. *Remote Sensing*, *15*(14), 3557. https://doi.org/10.3390/rs1514355

McRae, W. M., & Thomson, N. R. (2000). VLF phase and amplitude: Daytime ionospheric parameters. *Journal of Atmospheric and Solar-Terrestrial Physics*, *62*(7), 609–618. https://doi.org/10.1016/S1364-6826(00)00027-4

McRae, W. M., & Thomson, N. R. (2004). Solar flare induced ionospheric D-region enhancements from VLF phase and amplitude observations. *Journal of Atmospheric and Solar-Terrestrial Physics*, *66*(1), 77–87. https://doi.org/10.1016/j.jastp.2003.09.009

Mitra, A. P. (1974). *Ionospheric effects of solar flares* (Vol. 46, p. 307). Reidel.

Mitra, A. P. (1975). D-region in disturbed conditions, including flares and energetic particles. *Journal of Atmospheric and Terrestrial Physics*, *37*(6–7), 895–913. https://doi.org/10.1016/0021-9169(75)90005-7

Nickolaenko, A. P., & Hayakawa, M. (2002). Resonances in the earth-ionosphere cavity. *Springer Science and Business Media*, *19*.

Nieckarz, Z., Kulak, A., Zieba, S., & Odzimek, A. (2011). Cloud-to-ground lightning dipole moment from simultaneous observations by ELF receiver and combined direction finding and time-of-arrival lightning detection system. *Journal of Geophysical Research*, *116*(D8), D08107. https://doi.org/10.1029/2010JD014736

Schmitter, E. D. (2013). Modeling solar flare induced lower ionosphere changes using VLF/LF transmitter amplitude and phase observations at a midlatitude site. *Annales Geophysicae*, *31*(4), 765–773. Copernicus GmbH. https://doi.org/10.5194/angeo-31-765-2013

Thomson, N. R., & Clilverd, M. A. (2001). Solar flare induced ionospheric D-region enhancements from VLF amplitude observations. *Journal of Atmospheric and Solar-Terrestrial Physics*, *63*(16), 1729–1737. https://doi.org/10.1016/S1364-6826(01)00048-7

Thomson, N. R., Rodger, C. J., & Clilverd, M. A. (2005). Large solar flares and their ionospheric *D* region enhancements. *Journal of Geophysical Research*, *110*(A6), A06306. https://doi.org/10.1029/2005JA011008

Tsurutani, B. T., Verkhoglyadova, O. P., Mannucci, A. J., Lakhina, G. S., Li, G., & Zank, G. P. (2009). A brief review of "solar flare effects" on the ionosphere. *Radio Science*, *44*(1), RS0A17. https://doi.org/10.1029/2008RS004029

Verronen, P. T., Seppälä, A., Clilverd, M. A., Rodger, C. J., Kyrölä, E., Enell, C.-F., et al. (2005). Diurnal variation of ozone depletion during the October–November 2003 solar proton events. *Journal of Geophysical Research*, *110*(A9), A09S32. https://doi.org/10.1029/2004JA010932

Wait, J. R., & Spies, K. P. (1964). Characteristics of the earth-ionosphere waveguide for VLF radio waves. *NBS Tech. Note*, *300*. https://nvlpubs.nist.gov/nistpubs/Legacy/TN/nbstechnicalnote300.pdf

Wenzel, D., Jakowski, N., Berdermann, J., Mayer, C., Vallardes, C., & Heber, B. (2016). Global ionospheric flare detection system (GIFDS. *Journal of Atmospheric and Solar-Terrestrial Physics*, *138-139*, 233–242. https://doi.org/10.1016/j.jastp.2015.12.011